2012

CeO2 nanoparticles synthesized by a microwave-assisted hydrothermal method: evolution from nanospheres to nanorods

CRYSTENGCOMM, CAMBRIDGE, v. 14, n. 3, pp. 1150-1154, NOV-DEC, 2012
http://www.producao.usp.br/handle/BDPI/43317

CrystEngComm

Cite this: *CrystEngComm*, 2012, **14**, 1150

www.rsc.org/crystengcomm

PAPER

CeO_2 nanoparticles synthesized by a microwave-assisted hydrothermal method: evolution from nanospheres to nanorods

V. D. Araújo,*[a] W. Avansi,[a] H. B. de Carvalho,[b] M. L. Moreira,[c] E. Longo,[c] C. Ribeiro[d] and M. I. B. Bernardi[a]

Received 12th September 2011, Accepted 2nd November 2011
DOI: 10.1039/c1ce06188g

Ceria (CeO_2) plays a vital role in emerging technologies for environmental and energy-related applications. The catalytic efficiency of ceria nanoparticles depends on its morphology. In this study, CeO_2 nanoparticles were synthesized by a microwave-assisted hydrothermal method under different synthesis temperatures. The samples were characterized by X-ray diffraction, transmission electron microscopy, Raman scattering spectroscopy, electron paramagnetic resonance spectroscopy and by the Brunauer–Emmett–Teller method. The X-ray diffraction and Raman scattering results indicated that all the synthesized samples had a pure cubic CeO_2 structure. Rietveld analysis and Raman scattering also revealed the presence of structural defects due to an associated reduction in the valence of the Ce^{4+} ions to Ce^{3+} ions caused by an increasing molar fraction of oxygen vacancies. The morphology of the samples was controlled by varying the synthesis temperature. The TEM images show that samples synthesized at 80 °C consisted of spherical particles of about 5 nm, while those synthesized at 120 °C presented a mix of spherical and rod-like nanoparticles and the sample synthesized at 160 °C consisted of nanorods with 10 nm average diameter and 70 nm length. The microwave-assisted method proved to be highly efficient for the synthesis of CeO_2 nanoparticles with different morphologies.

Introduction

Ceria (CeO_2) nanostructures have attracted the interest of many researchers in the past decade due to their great potential for applications in catalysis, electrochromic devices, gas sensors, ultraviolet ray detectors, environmentally friendly pigments, gamma radiation dosimetry, *etc.*[1] CeO_2 is a chemically stable oxide, with an outstanding capacity to store or release oxygen due to the variation of the oxidation state of cerium between +3 and +4, under various reductive or oxidizing conditions.[2] For example, the catalytic activity of oxides is linked to their capability of providing adsorbent oxygen species at their surfaces and an easy extraction of their lattice oxygen forming oxygen vacancies.[2]

The technological applications of nanostructured materials are strongly related to their crystalline structure, crystal size and morphology.[3,4] For CeO_2 nanostructures, Tana *et al.*[5] reported higher catalytic activity for CO oxidation and oxygen storage capacity of CeO_2 nanowires than nanorods and nanoparticles. Si and Flytzani-Stephanopoulos[6] observed a strong shape/crystal plane effect of CeO_2 on the gold–ceria activity for the WGS reaction. They have reported that the rod-like ceria enclosed by {110} and {100} planes is most active for gold stabilization/activation. Li *et al.*[1] verified that CeO_2 nanowires could be used in dosimetry for low radiation dose, since nanowire dosimetry possessed high sensitivity while retaining cost-effectiveness as the conventional chemical dosimeters. CeO_2 nanorod arrays were successfully grown on Ti substrates by an electrochemical assembly process which exhibited photovoltaic response under visible light illumination, creating the opportunity to build various photoelectrochemical devices.[7] Lin and Chowdhury[8] published a review on nanostructured cerium oxide and its various applications, especially several industrially important reactions, including low-temperature CO oxidation, UV absorbing semiconductor materials, partial oxidation of hydrocarbons, hydrogenation of carbon oxides, and wastewater treatment. In this context, several strategies have been developed to obtain CeO_2 nanostructures with different morphologies, *e.g.*, hydrothermal and solvothermal,[9–11] microwave-assisted hydrothermal,[12,13] microemulsion,[14,15] impregnation,[14] coprecipitation,[16] urea–nitrate combustion,[17] sol–gel[18–20] and metal–organic chemical vapor deposition (MOCVD)[21–24] methods. Among these methods, hydrothermal treatments appear to be potentially interesting in terms of morphological variations.[25–31] Guan *et al.* reported a systematic study of ceria materials with different morphologies such as sphere, rods, and prisms *via* the hydrolysis of solutions containing $Ce(NO_3)_3$ and urea under hydrothermal conditions.[32] According to these authors, different

[a]*Instituto de Física de São Carlos, USP—Universidade de São Paulo, Av. Trabalhador São-carlense, 400, São Carlos, 13560-970, SP, Brazil. E-mail: dantas@ursa.ifsc.usp.br; Fax: +55 16 3373-9824; Tel: +55 16 3373-9828*
[b]*Universidade Federal de Alfenas, 37130-000 Alfenas, Minas Gerais, Brazil*
[c]*INCTMN, LIEC, Instituto de Química, UNESP, R. Francisco Degni, s/n, CEP 14800-900 Araraquara, SP, Brazil*
[d]*National Nanotechnology Laboratory for Agribusiness (LNNA), Embrapa Agricultural Instrumentation, 13560-970 São Carlos, SP, Brazil*

morphologies were obtained by carefully adjusting the synthesis conditions such as salt concentration, temperature and synthesis time. As an improvement of the method, the microwave-assisted route has the advantage of shorter reaction times, production of small particles with a narrow size distribution and high purity.[12] According to Godinho *et al.* microwave irradiation increases the effective collision rate, reducing the time required to obtain anisotropically grown nanostructures.[33]

Based on these trends, the aim of the work described here is to verify the effect of intrinsic parameters that can be controlled during microwave-assisted hydrothermal synthesis, such as temperature and time, on the evolution of CeO_2 nanostructures. We also demonstrate that the morphology of the CeO_2 anisotropic nanostructure is governed by the oriented attachment (OA) growth mechanism.

Experimental

In a typical procedure to obtain CeO_2 nanostructures, 0.02 mol of cerium nitrate ($Ce(NO_3)_2 \cdot 6H_2O$) was dissolved in 50 mL of distilled water. Then, 50 mL of a 5 M NaOH solution was added rapidly under vigorous stirring. The mixed solution was placed in a 110 mL Teflon autoclave reaching 90% of its volume, which was sealed and placed in a microwave hydrothermal system, applying 2.45 GHz of microwave radiation at a maximum power of 800 W. The as-prepared solution was subjected to the microwave hydrothermal synthesis temperatures of 80, 120 and 160 °C for 16 min at a heating rate of 30 °C·min^{-1} and then air-cooled at room temperature. The as-obtained precipitate powder was washed several times with distilled water and isopropyl alcohol and then dried at 60 °C for 24 h.

The powders were characterized structurally in an X-ray diffractometer (Rigaku, Rotaflex RU200B) with CuKα radiation (50 kV, 100 mA, $\lambda = 1.5405$ Å), using a $\theta - 2\theta$ configuration and a graphite monochromator. The scanning range was between 20 and 90° (2θ), with a step size of 0.02° and a step time of 5.0 s. A Rietveld analysis was performed using the Rietveld refinement program GSAS.[34] A pseudo-Voigt profile function was used. The specific surface area was estimated from the N_2 adsorption/desorption isotherms at liquid nitrogen temperature, using a Micromeritics ASAP 2000 particle size analyzer and applying the Brunauer–Emmett–Teller (BET) method. The size and morphology of the samples were determined by transmission electron microscopy (TEM) using a JEOL JEM 2010 URP, operating at 200 keV. Raman spectroscopy was carried out at room temperature in a Jobin-Yvon-64000 micro-Raman system in the backscattering geometry, using the 488 nm line of an Ar^+ laser for excitation. We used an optical lens with 100× magnification, which supplies an average laser spot size of 1 μm. The EPR spectra were recorded at 20 K in an X-band Bruker ELEXSYS E580 spectrometer. The temperature was controlled by an Oxford ITC503 cryogenic system. The spectra were obtained at a modulation frequency of 100 kHz, a modulation amplitude of 0.2 mT and a microwave power of 1 mW.

Results and discussion

Fig. 1 shows the XRD patterns of the CeO_2 samples obtained. Fluorite type CeO_2 (ICSD no. 156250) was present in all the samples. No secondary phase peaks were found in the samples. Table 1 describes the lattice parameter a calculated from the Rietveld refinement. The samples synthesized by the microwave-assisted method presented a higher a value than the bulk CeO_2 (5.4116(1) Å, ICSD no. 156250). The increasing lattice constant (strain relative to the bulk) for successively smaller particles in CeO_2 is explained in terms of an associated reduction in the valence of the Ce^{4+} ions to Ce^{3+} ions caused by an increasing molar fraction of oxygen vacancies.[35] Fig. 2 presents the EPR spectra of the samples. Pure CeO_2 revealed the formation of one type of paramagnetic species, A, due to Ce^{3+} (centered around 3445 G).[36] This result corroborates the assumption of the presence of Ce^{3+} ions and oxygen vacancies in the samples.[35]

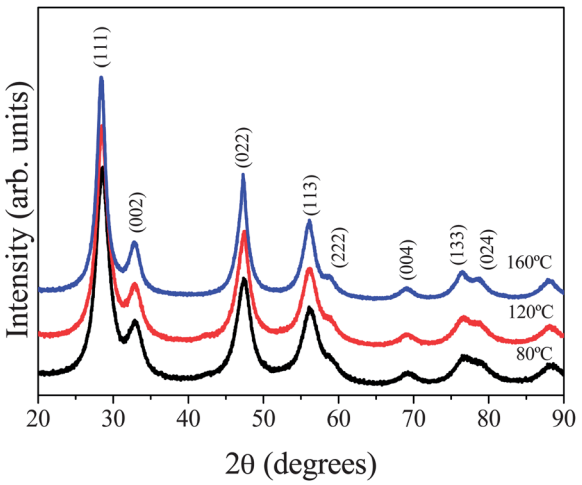

Fig. 1 XRD patterns of CeO_2 samples synthesized at 80, 120 and 160 °C.

In heterogeneous catalysis, it is well known that the catalytic activity of a supported metal increases with increasing surface area.[37] Table 1 also presents the BET specific surface area for the samples. Materials with a high surface area of up to 144 m^2 g^{-1} were obtained. A linear decrease in the specific surface area of the samples with increasing synthesis temperature is observed, indicating an increase in particle size for higher synthesis temperatures.

Fig. 3 shows Raman spectra of the samples, complementing the structural characterization. Dioxides with a fluorite structure have only one allowed Raman mode, which has an F_{2g} symmetry and can be viewed as a symmetric breathing mode of the O atoms around each cation.[38] In bulk CeO_2 this frequency is 465 cm^{-1}. We observed two main features centered at 456 and 600 cm^{-1}.

Table 1 Specific surface area (S_{BET}), lattice parameter (a), frequency shift of main Raman peak ($\Delta\omega_{exp}$) and calculated frequency shift of the main Raman peak ($\Delta\omega$) in CeO_2 synthesized *via* the microwave-assisted hydrothermal method

Synthesis temperature/°C	S_{BET}/m^2 g^{-1}	a^a/Å	$\Delta\omega_{exp}$/cm^{-1}	$\Delta\omega^b$/cm^{-1}
80	144	5.435(9)	−9	−9
120	117	5.442(4)	−10.4	−11
160	87	5.440(9)	−8.2	−11

[a] Calculated *via* Rietveld refinement. [b] Calculated according to ref. 38.

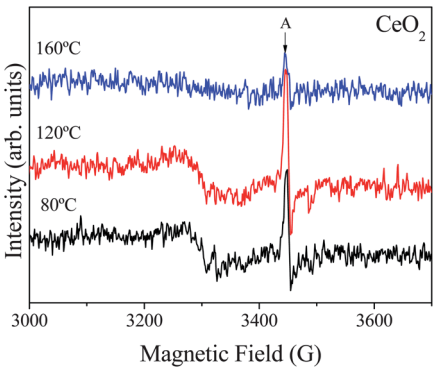

Fig. 2 EPR spectra of CeO_2 samples synthesized at different temperatures.

The former is assigned to the fluorite F_{2g} mode, confirming the XRD results. The broad band around 600 cm^{-1} can be ascribed to oxygen vacancies and defects caused by small size effects.[38]

The samples presented a shift of the F_{2g} mode to lower frequencies than those of the bulk (inset of Fig. 3 and also presented in Table 1). According to Spanier *et al.*,[35] several factors can contribute to the changes in the Raman peak position and linewidth of the 465 cm^{-1} peak, including phonon confinement, strain, broadening associated with size distribution, defects, and variations in phonon relaxation as a function of particle size. Considering the change in lattice constant, the frequency shift $\Delta\omega$ of the Raman mode produced by a change in lattice constant Δa can be written in terms of the Grüneisen parameter as $\Delta\omega = -3\gamma\omega_0\Delta a/a_0$, where ω_0 is the Raman frequency in pure CeO_2, a_0 is the CeO_2 lattice constant, and γ is the Grüneisen constant.[38] This frequency shift was calculated with $\omega_0 = 465$ cm^{-1}, $a_0 = 0.54116(1)$ nm and $\gamma = 1.24$.[35] These theoretical results are presented in Table 1 and are in good agreement with the experimental values.

Fig. 4 presents HRTEM and TEM images of the CeO_2 nanoparticles. The HRTEM image in Fig. 4a indicates that the samples synthesized at 80 °C are composed mainly of nanospheres (indicated by black arrows) with an average size of 5 nm. From an analysis of the expanded HRTEM image, inset in Fig. 4a, one can see that the distance between neighboring planes

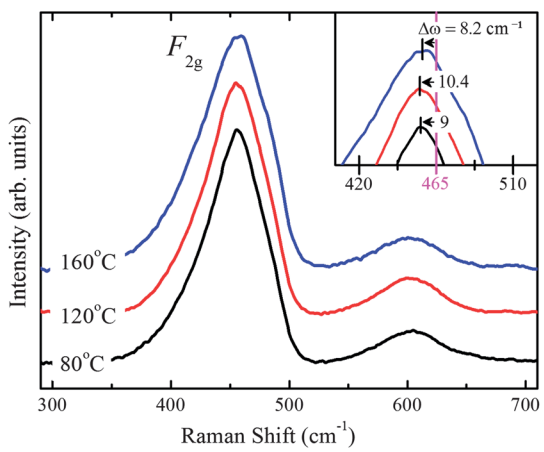

Fig. 3 Raman spectra of CeO_2 samples synthesized at different temperatures. The inset shows the frequency shift in the bulk F_{2g} mode.

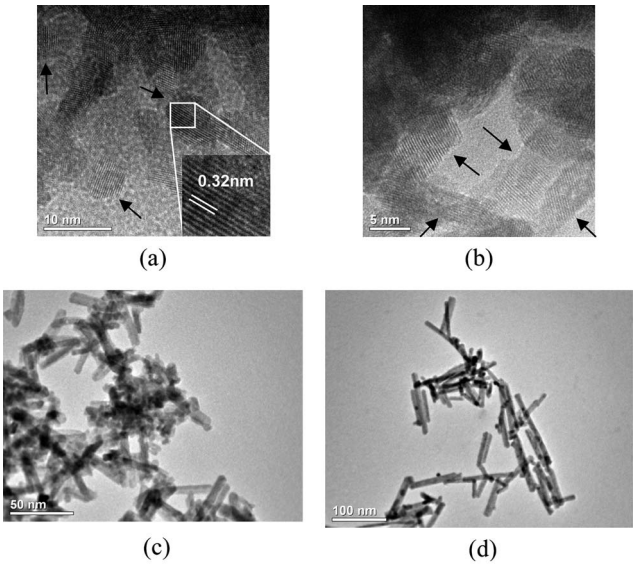

Fig. 4 HRTEM images of the as-obtained samples synthesized at 80 °C reveal that the samples are composed of (a) nanospheres with an average size of 5 nm and (b) nanostructures with a poor morphology. Black arrows indicate these structures. TEM images of samples synthesized at: (c) 120 and (d) 160 °C.

is about 0.32 nm, related to the (111) crystallographic plane of cubic CeO_2. The presence of the (111) crystallographic plane of cubic CeO_2 confirms that the nanospheres are CeO_2 related structures. Some anisotropic nanostructures with a poor morphology (indicated by black arrows) are also visible in these samples, as shown in Fig. 4b. The TEM image of the sample synthesized at 120 °C, Fig. 4c, reveals a mixture of morphologies composed mainly of nanorods with some nanospheres, with diameters around 5 and 7 nm, respectively. Since the sizes of the sample prepared at 80 °C (mainly nanospheres) are quite similar, this result shows that the increase of the synthesis temperature from 80 to 120 °C is mainly implicated in morphological changes than in regular crystal growth, as shown in Fig. 4. The samples synthesized at 160 °C, Fig. 4d, showed the presence of nanorods with an average diameter of 10 nm and a length of 70 nm; a few nanospheres were also observed.

From the images in Fig. 4 one can infer that the anisotropic nanostructures with a poor morphology (Fig. 4b) evolve to well-defined nanorods as the temperature of synthesis increases. The Ostwald Ripening (OR) model, which is a dissolution–reprecipitation growth mechanism, cannot be considered the only growth mechanism of those structures, since the extensive presence of line defects would not be expected in this case.[39–41] One has to consider the oriented attachment (OA) mechanism, which has been proved effective in tailoring anisotropic particles.[39,42–46] In fact, the mechanism was previously observed for CeO_2. Cao *et al.*[13] showed that the increase in size and changes in the morphology of CeO_2 nanostructures prepared by the microwave-assisted hydrothermal method could be described by the Ostwald ripening coupled self-assembly process.

Fig. 5 presents HRTEM images of the entire set of samples. Fig. 5a and b indicate that the anisotropic nanostructures are composed of oriented primary spherical nanoparticles. In the

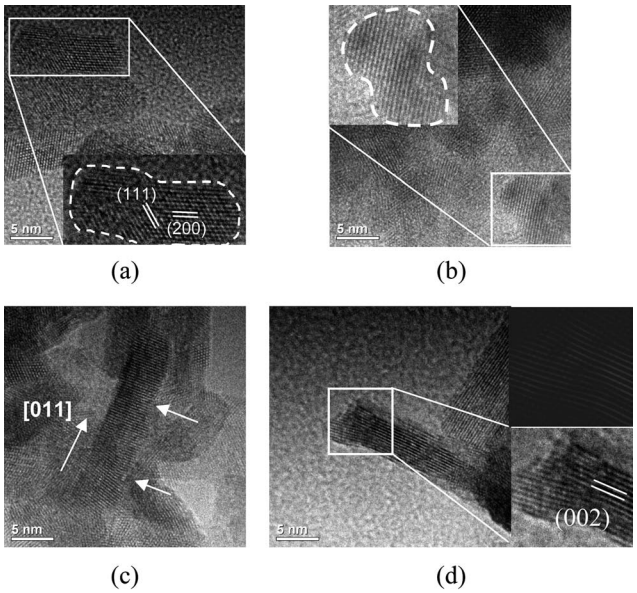

Fig. 5 HRTEM images of the as-obtained samples synthesized at: (a) 80 °C; (b and c) at 120 °C; and (d) 160 °C. The insets show crystallographic planes and directions (a and d), and neck formation (b). White arrows indicate the plane direction.

final formation of these structures, a certain degree of diffusion-driven surface accommodation may be possible at longer treatment times, ensuring the rod-like aspect. The arrows in Fig. 5c indicate the presence of defects in the interfacial attachment region of the primary particles. This finding, *i.e.*, the aggregation of several nanocrystals with similar crystallographic orientations originating anisotropic structures, as well as the presence of some defects, is strong evidence that the OA process is the effective growth mechanism of the samples obtained under microwave-assisted hydrothermal conditions. Several papers have shown that, for the OA mechanism, when particle-to-particle contact occurs in a particular crystallographic orientation, the coalescence of nanoparticles leads to the formation of defects such as dislocations and/or twin boundaries at the interface between the nanoparticles.[33,43,46–49] Additionally, Fig. 5c and d show that the as-obtained nanorods possess single-crystal nature. Fig. 5d reveals the presence of nanospheres attached to nanorods in the same crystallographic plane for the sample synthesized at 160 °C. In fact, the reconstructed lattice image of the area indicated in Fig. 5d shows an imperfect attachment that would lead to a defective structure. Fig. 5a and d also indicate that the nanostructures appear to grow along the length of the (111) crystallographic plane and along the diameter of the (002) plane. This crystallographic information indicates the formation of nanorods with preferential growth in the [110] direction.[33] This directional growth is in agreement with the fact that the driving force for the coalescence process in the OA mechanism is related to the reduction of surface energy, aimed at minimizing the area of high-energy faces.[33,39,40,44–46,48] In a cubic system, growth along the {110} plane is expected since the {111} plane is the more stable one.[33] Godinho *et al.* reported a similar result, demonstrating that oriented attachment was the dominant mechanism responsible for the anisotropic growth of gadolinium-doped ceria nanorods.[33]

From our experimental results it is clear that the synthesis temperature plays an important role in obtaining well-defined anisotropic CeO_2 nanostructures under microwave-assisted hydrothermal conditions. Lee *et al.*[49] showed that the increase of synthesis temperature plays an important role in increasing the degree of coalescence in the OA mechanism, which may be related to increased nanoparticle mobility, and hence, collision frequency. This explains the anisotropic structures with a poor morphology observed at the lowest synthesis temperature (80 °C), while the samples processed at 160 °C showed well defined nanorods. It should be noted that, although the OA mechanism is attributed as the main factor of anisotropic formation, a certain degree of diffusional motion can occur in higher temperatures, leading to the OR mechanism as concomitant to OA. In fact, both mechanisms may occur, but the OR mechanism is an equilibrium condition which is expected to be attained at longer times, smoothing the surface of the pre-formed rods.[39]

Conclusion

The microwave-assisted hydrothermal method proved to be efficient in the synthesis of CeO_2 nanoparticles with different morphologies. Control of the morphology was achieved by varying the synthesis temperature. Nanospheres evolved to nanorods with increasing synthesis temperature. The presence of structural defects was detected by Rietveld analysis and optical characterization and was attributed to an associated reduction in the valence of Ce^{4+} ions to Ce^{3+} ions caused by the increasing molar fraction of oxygen vacancies.

Acknowledgements

The authors gratefully acknowledge the financial support of the Brazilian research funding agencies FAPESP and CNPq. We also thank the Electron Microscopy Laboratory (LME) of the Brazilian National Synchrotron Light Laboratory (LNLS) for the use of its HRTEM microscopy facility. Special thanks go to Prof. Dr Otaciro Rangel for his contribution to this work, and particularly to Dr José Fernando de Lima for the EPR measurements.

References

1 Y. Li, X. Dong, J. Gao, D. Hei, X. Zhou and H. Zhang, *Phys. E*, 2009, **41**, 1550–1553.
2 A. Kopia, K. Kowalski, M. Chmielowska and C. Leroux, *Surf. Sci.*, 2008, **602**, 1313–1321.
3 Y. Wang and G. Cao, *Chem. Mater.*, 2006, **18**, 2787–2804.
4 C. N. R. Rao and A. K. Cheetham, *J. Mater. Chem.*, 2001, **11**, 2887–2894.
5 Tana, M. Zhang, J. Li, H. Li, Y. Li and W. Shen, *Catal. Today*, 2009, **148**, 179–183.
6 R. Si and M. Flytzani-Stephanopoulos, *Angew. Chem., Int. Ed.*, 2008, **47**, 2884–2887.
7 X. Lu, D. Zheng, P. Zhang, C. Liang, P. Liu and Y. Tong, *Chem. Commun.*, 2010, **46**, 7721–7723.
8 K.-S. Lin and S. Chowdhury, *Int. J. Mol. Sci.*, 2010, **11**, 3226–3251.
9 X. S. Wu and S. Kawi, *Cryst. Growth Des.*, 2010, **10**, 1833–1841.
10 M.-M. Titirici, M. Antonietti and A. Thomas, *Chem. Mater.*, 2006, **18**, 3808–3812.
11 G. Chen, C. Xu, X. Song, S. Xu, Y. Ding and S. Sun, *Cryst. Growth Des.*, 2008, **8**, 4449–4453.
12 F. Gao, Q. Lu and S. Komarneni, *J. Nanosci. Nanotechnol.*, 2006, **6**, 3812–3819.

13 C.-Y. Cao, Z.-M. Cui, C.-Q. Chen, W.-G. Song and W. Cai, *J. Phys. Chem. C*, 2010, **114**, 9865–9870.
14 D. Gamarra, C. Belver, M. Fernández-García and A. Martínez-Arias, *J. Am. Chem. Soc.*, 2007, **129**, 12064–12065.
15 B. Suresh, *et al.*, *Nanotechnology*, 2009, **20**, 085713.
16 G. Avgouropoulos, T. Ioannides and H. Matralis, *Appl. Catal., B*, 2005, **56**, 87–93.
17 G. Avgouropoulos and T. Ioannides, *Appl. Catal., A*, 2003, **244**, 155–167.
18 D. Potemkin, P. Snytnikov, V. Pakharukova, G. Semin, E. Moroz and V. Sobyanin, *Kinet. Catal.*, 2010, **51**, 119–125.
19 G. Avgouropoulos, T. Ioannides, C. Papadopoulou, J. Batista, S. Hocevar and H. K. Matralis, *Catal. Today*, 2002, **75**, 157–167.
20 V. D. Araújo and M. I. B. Bernardi, *J. Therm. Anal. Calorim.*, 2010, 1–6.
21 R. Lo Nigro, R. Toro, G. Malandrino and I. L. Fragalà, *Chem. Mater.*, 2003, **15**, 1434–1440.
22 R. Lo Nigro, R. G. Toro, G. Malandrino and I. L. Fragala, *J. Mater. Chem.*, 2005, **15**, 2328–2337.
23 D. Barreca, E. Comini, A. Gasparotto, C. Maccato, C. Maragno, G. Sberveglieri and E. Tondello, *J. Nanosci. Nanotechnol.*, 2008, **8**, 1012–1016.
24 D. Barreca, A. Gasparotto, C. Maccato, C. Maragno and E. Tondello, *Langmuir*, 2006, **22**, 8639–8641.
25 S. P. Pang, G. C. Li, L. Wang and Z. K. Zhang, *J. Cryst. Growth*, 2006, **293**, 423–427.
26 F. Zhou, X. M. Zhao, C. G. Yuan and L. Li, *Cryst. Growth Des.*, 2008, **8**, 723–727.
27 W. Avansi, C. Ribeiro, E. R. Leite and V. R. Mastelaro, *Cryst. Growth Des.*, 2009, **9**, 3626–3631.
28 B. X. Li, Y. Xu, G. X. Rong, M. Jing and Y. Xie, *Nanotechnology*, 2006, **17**, 2560–2566.
29 C. Ribeiro, C. M. Barrado, E. R. Camargo, E. Longo and E. R. Leite, *Chem.–Eur. J.*, 2009, **15**, 2217–2222.
30 R. L. Penn and J. F. Banfield, *Geochim. Cosmochim. Acta*, 1999, **63**, 1549–1557.
31 M. Yoshimura and K. Byrappa, *J. Mater. Sci.*, 2008, **43**, 2085–2103.
32 Y. Guan, E. Hensen, Y. Liu, H. Zhang, Z. Feng and C. Li, *Catal. Lett.*, 2010, **137**, 28–34.
33 M. Godinho, C. Ribeiro, E. Longo and E. R. Leite, *Cryst. Growth Des.*, 2008, **8**, 384–386.
34 A. C. Larson and R. B. V. Dreele, in *Los Alamos National Laboratory Report LAUR 86-748*, 1994.
35 J. E. Spanier, R. D. Robinson, F. Zhang, S.-W. Chan and I. P. Herman, *Phys. Rev. B: Condens. Matter Mater. Phys.*, 2001, **64**, 245407.
36 P. Ratnasamy, D. Srinivas, C. V. V. Satyanarayana, P. Manikandan, R. S. Senthil Kumaran, M. Sachin and V. N. Shetti, *J. Catal.*, 2004, **221**, 455–465.
37 J. L. Carter, J. A. Cusumano and J. H. Sinfelt, *J. Phys. Chem.*, 1966, **70**, 2257–2263.
38 J. R. McBride, K. C. Hass, B. D. Poindexter and W. H. Weber, *J. Appl. Phys.*, 1994, **76**, 2435–2441.
39 C. Ribeiro, E. J. H. Lee, E. Longo and E. R. Leite, *ChemPhysChem*, 2005, **6**, 690–696.
40 C. Ribeiro, E. J. H. Lee, E. Longo and E. R. Leite, *ChemPhysChem*, 2006, **7**, 664–670.
41 A. P. Alivisatos, *J. Phys. Chem.*, 1996, **100**, 13226–13239.
42 C. Ribeiro, C. Vila, D. B. Stroppa, V. R. Mastelaro, J. Bettini, E. Longo and E. R. Leite, *J. Phys. Chem. C*, 2007, **111**, 5871–5875.
43 C. Ribeiro, C. Vila, J. M. E. de Matos, J. Bettini, E. Longo and E. R. Leite, *Chem.–Eur. J.*, 2007, **13**, 5798–5803.
44 R. L. Penn and J. F. Banfield, *Am. Mineral.*, 1998, **83**, 1077–1082.
45 X. G. Peng, L. Manna, W. D. Yang, J. Wickham, E. Scher, A. Kadavanich and A. P. Alivisatos, *Nature*, 2000, **404**, 59–61.
46 R. L. Penn and J. F. Banfield, *Science*, 1998, **281**, 969–971.
47 W. Avansi, C. Ribeiro, E. R. Leite and V. R. Matelaro, *J. Cryst. Growth*, 2010, **312**, 3555–3559.
48 J. F. Banfield, S. A. Welch, H. Z. Zhang, T. T. Ebert and R. L. Penn, *Science*, 2000, **289**, 751–754.
49 E. J. H. Lee, C. Ribeiro, E. Longo and E. R. Leite, *Chem. Phys.*, 2006, **328**, 229–235.